

RESEARCH ARTICLE | SEPTEMBER 19 2023

Error-field penetration thresholds in ohmically heated ITER and SPARC plasmas

R. Fitzpatrick  

 Check for updates

Phys. Plasmas 30, 092512 (2023)

<https://doi.org/10.1063/5.0161860>


View
Online


Export
Citation

CrossMark

Physics of Plasmas

Features in Plasma Physics Webinars

Register Today!

Error-field penetration thresholds in ohmically heated ITER and SPARC plasmas

Cite as: Phys. Plasmas **30**, 092512 (2023); doi: [10.1063/5.0161860](https://doi.org/10.1063/5.0161860)

Submitted: 12 June 2023 · Accepted: 24 August 2023 ·

Published Online: 19 September 2023



View Online



Export Citation



CrossMark

R. Fitzpatrick^{a)} 

AFFILIATIONS

Institute for Fusion Studies, Department of Physics, University of Texas at Austin, Austin, Texas 78712, USA

^{a)} Author to whom correspondence should be addressed: rfitzp@utexas.edu

ABSTRACT

The critical $n = 1$, $n = 2$, and $n = 3$ error-field amplitudes needed to trigger error-field penetration in ITER and SPARC, steady-state, ohmically heated plasmas are calculated using a standard asymptotic matching approach. The calculation incorporates plasma impurities, trapped particles, the bootstrap current, and neoclassical poloidal flow-damping. The energy confinement time is specified by the neo-Alcator scaling law in the low-density linear Ohmic confinement (LOC) regime and by the ITER-89P L-mode scaling law in the high-density saturated Ohmic confinement (SOC) regime. The response of the plasma in the inner region is calculated using a linearized version of the four-field model. At the normal operating electron number density, diamagnetic levels of rotation are found to be sufficient to protect ITER and SPARC ohmically heated plasmas from $m = 2/n = 1$ error-field penetration. On the other hand, SPARC, and especially ITER, ohmically heated plasmas may be vulnerable to $n > 1$ error-field penetration. ITER and SPARC ohmically heated plasmas are also slightly more susceptible to error-field penetration when the electron fluid at the rational surface rotates in the ion diamagnetic direction, rather than the electron diamagnetic direction. At electron number densities that are sufficiently low that the plasma lies in the LOC confinement regime, the error-field penetration threshold increases with increasing density. However, as soon as the electron number density becomes large enough that the plasma enters the SOC regime, the increase in the error-field penetration threshold with increasing density levels off.

Published under an exclusive license by AIP Publishing. <https://doi.org/10.1063/5.0161860>

I. INTRODUCTION

Error-fields in tokamaks are a type of static (in the laboratory frame) non-axisymmetric magnetic perturbation that usually originates from imperfections in magnetic field-coils. An error-field whose amplitude (δB) is smaller than that of the equilibrium magnetic field (B) by many orders of magnitude (i.e., $\delta B/B \simeq 10^{-4}$) can drive a comparatively wide (i.e., a few percent of the plasma minor radius) locked (i.e., non-rotating) helical magnetic island chain, also known as a locked mode, inside a tearing-stable tokamak plasma.^{1–14} This behavior is of grave concern because the occurrence of locked modes in tokamak plasmas is very strongly correlated with disruptive losses of energy, momentum, and particle confinement.¹⁵ Although most previous research has concentrated on the detrimental effects of $n = 1$ (where n is the toroidal mode number) error-fields, there is a growing concern about the effects of $n > 1$ error-fields.¹⁶ This is particularly the case because deliberately applied $n > 1$ error-fields, known as resonant magnetic perturbations (RMPs), are often used to control dangerous edge localized modes (ELMs) in tokamak plasmas.^{17–20}

The physics of error-field-driven magnetic reconnection in a tokamak plasma is well known^{21–24} but is worth recapitulating in this

introduction. A helical error-field with m periods in the poloidal direction and n periods in the toroidal direction resonates with the plasma at the so-called rational magnetic flux-surface at which the safety-factor takes the value m/n . As far as its response to a small-amplitude error-field is concerned, a high Lundquist number tokamak plasma can be divided into two regions. The so-called inner region lies in the immediate vicinity of the rational surface. The so-called outer region comprises everywhere in the plasma apart from the inner region as well as the vacuum region surrounding the plasma. The response of the plasma to the error-field in the outer region is governed by the equations of linear, marginally stable, ideal magnetohydrodynamics (MHD). The minimal model that can realistically describe the response of the plasma in the inner region should contain plasma resistivity, $\mathbf{E} \times \mathbf{B}$ flows, electron and ion diamagnetic flows, the ion sound radius, and anomalous cross-flux-surface transport of energy and momentum. It is important to include diamagnetic flows in the model because they are similar in magnitude to $\mathbf{E} \times \mathbf{B}$ flows in an ohmically heated plasma (which is the type of plasma considered in this paper). It is important to include the ion sound radius in the model because the response of the ion fluid to the error-field is

radically different to that of the electron fluid on length-scales below the ion sound radius. Finally, it is important to include realistic levels of perpendicular energy and momentum transport in the model because these effects significantly change the response of the inner region to the error-field. Plasma flows in the inner region lead to the development of a localized shielding current that suppresses driven magnetic reconnection at the rational surface. However, the error-field exerts a localized electromagnetic torque in the inner region that acts to modify the plasma flows in such a manner as to reduce the shielding current. If the error-field amplitude is gradually ramped up, then a critical error-field amplitude is reached at which there is a sudden shift in the plasma flows, leading to the complete elimination of the shielding current and allowing unhindered driven magnetic reconnection. This phenomenon is known as error-field penetration.

Conventional tokamak plasmas are initiated in a Ohmic phase in which the dominant energy input to the plasma comes from Joule heating. Ohmic plasmas are particularly vulnerable to error-field penetration because of their comparatively low temperatures and comparatively low levels of plasma rotation. The aim of this paper is to estimate the critical error-field amplitude required to induce penetration in an ITER²⁵ or a SPARC²⁶ steady-state, ohmically heated plasma.

The standard approach to estimating the error-field penetration threshold in an ITER or a SPARC ohmically heated plasma is by means of scaling studies using either empirical data from existing tokamaks²⁷ or data from computer simulations.²⁸ In this paper, we shall adopt a different approach in which we shall attempt to directly simulate an ITER or a SPARC steady-state, ohmically heated plasma. Simulating a steady-state, ohmically heated tokamak plasma turns out to be a particularly simple task because the heating source is a known quantity. The two quantities whose values are the most uncertain in ITER or SPARC ohmically heated plasmas are the energy confinement time and the $\mathbf{E} \times \mathbf{B}$ rotation level. However, the scaling of the energy confinement time with plasma parameters has been the subject of extensive previous research.²⁹ Consequently, we can extrapolate the confinement time from existing tokamaks to ITER or SPARC with some degree of confidence. Moreover, for the case of an ohmically heated tokamak plasma, there is no reason to suppose that the level of $\mathbf{E} \times \mathbf{B}$ rotation will be substantially different from the level of diamagnetic rotation,³⁰ which allows us to make an educated guess as to the likely range of $\mathbf{E} \times \mathbf{B}$ rotation levels in ITER or SPARC ohmically heated plasmas.

For the sake of simplicity, our model plasma equilibrium employs cylindrical geometry. However, we have endeavored to make the calculation of the Ohmic heating power as realistic as possible by taking into account plasma impurities, trapped particles, the bootstrap current, and the correction to the conventional cylindrical expression for the safety-factor due to toroidicity and plasma shaping (see Sec. II).^{31–34}

Our model energy confinement time is specified by the neo-Alcator scaling law^{35,36} in the low-density linear Ohmic confinement (LOC) regime and by the ITER-89P L-mode scaling law^{29,37} in the high-density saturated Ohmic confinement (SOC) regime (see Sec. II).

The response of the plasma in the inner region is calculated using a linearized version of the four-field model³⁸ that contains seven parameters (corresponding to the local electron diamagnetic flow, the ion diamagnetic flow, the $\mathbf{E} \times \mathbf{B}$ flow, the ion sound radius, the anomalous cross field energy diffusivity, the anomalous cross field momentum diffusivity, and the Lundquist number)^{23,24} (see Sec. IV). It is a

reasonable approach to employ linear theory because prior to error-field penetration, driven magnetic reconnection is strongly suppressed by plasma flows,²¹ causing the driven island width to be less than the linear layer width (which is the condition for the validity of linear theory) (see Fig. 3). It is important to employ a two-fluid model of the resonant plasma response because conventional resistive-magnetohydrodynamics (MHD) is a completely inadequate resonant response model.

Our linear resonant response model does not incorporate the Glasser–Greene–Johnson (GGJ) effect^{39,40} because, as was demonstrated in Refs. 41 and 42, when realistic levels of anomalous cross field transport are included in the layer response calculation, this effect is reduced to such an extent that it does not contribute significantly to the layer response. (Of course, there is still a nonlinear GGJ effect that gives rise to a significant stabilizing term in the generalized Rutherford equation that scales as the inverse of the island width.⁴³ However, this term depends crucially on the flattening of the plasma pressure within the island separatrix and essentially disappears as soon as the island becomes too thin to effect such a flattening.⁴¹)

Our linear resonant response model also does not incorporate the perturbed bootstrap current^{44,45} because the linear layer width is much narrower than the width of a banana orbit (implying that the bootstrap current would not respond to the perturbed structure of the resonant layer).

The response of the plasma in the outer region is calculated self-consistently from the cylindrical tearing mode equation (see Sec. III).²¹

Finally, we calculate the response of the plasma to the localized electromagnetic torque that develops in the inner region by solving the full plasma angular equations of motion, taking the neoclassical damping of poloidal rotation into account.⁴⁶ The ultimate result is a torque balance equation that allows the local plasma flows, as well as the amount of reconnected magnetic flux driven at the rational surface, to be calculated as functions of the error-field amplitude (see Sec. V).

II. OHMICALLY HEATED TOKAMAK PLASMAS

A. Introduction

The aim of this section is to calculate the properties of a plasma confined in an idealized, steady-state, ohmically heated tokamak.

B. Plasma equilibrium

Our tokamak equilibrium is approximated as a periodic cylinder of circular cross section. Let us employ a conventional set of right-handed cylindrical coordinates, r , θ , and z . The equilibrium magnetic flux-surfaces lie on surfaces of constant r . The system is assumed to be periodic in the z (“toroidal”) direction, with periodicity length $2\pi R_0$, where R_0 is the simulated major radius of the plasma. It is helpful to define the simulated toroidal angle $\varphi = z/R_0$. Let a be the minor radius of the plasma. The equilibrium magnetic field is written $\mathbf{B} = B_\theta(r) \mathbf{e}_\theta + B_\varphi \mathbf{e}_z$, where $B_\theta(r)$ is the poloidal magnetic field-strength and B_φ is the (approximately) spatially uniform toroidal magnetic field-strength. The equilibrium current density takes the form $\mathbf{j} = j_\varphi(r) \mathbf{e}_z$.

C. Plasma energy balance

Suppose that the plasma consists of electrons, singly charged majority ions, and impurity ions. Let $p(r) = (1 + i_i) n_e T_e(r)$ be the total equilibrium plasma pressure profile (neglecting the contribution

from impurity ions), where $T_e(r)$ is the electron temperature profile, t_i is an assumed spatially uniform ratio of the ion to the electron temperature, and n_e is an assumed spatially uniform electron number density.

Suppose that the plasma is in a quasi-steady-state characterized by a spatially uniform parallel inductive electric field, E_{\parallel} . The electron energy balance equation is written as^{47,48}

$$\nabla \cdot (-\kappa_{\perp e} \nabla T_e) = \sigma_{\parallel} E_{\parallel}^2, \quad (1)$$

where $\kappa_{\perp e}$ is the perpendicular (to magnetic flux-surfaces) electron thermal conductivity and σ_{\parallel} is the parallel (to the magnetic field) plasma electrical conductivity.^{47,48} Let $\kappa_{\perp e} = n_e \chi_E$, where χ_E is an assumed spatially uniform perpendicular energy diffusivity. It follows that

$$\nabla^2 T_e = -\frac{\sigma_{\parallel} E_{\parallel}^2}{\chi_E n_e}. \quad (2)$$

Now, assuming that the plasma lies in the banana collisionality regime,^{31,32,49,50}

$$\sigma_{\parallel} = \frac{n_e e^2 \tau_e}{m_e Z'_{\text{eff}} \hat{\mu}_e}, \quad (3)$$

where

$$\tau_e = \frac{6\sqrt{2} \pi^{3/2} \epsilon_0^2 m_e^{1/2} T_e^{3/2}}{\ln \Lambda e^4 n_e}, \quad (4)$$

$$Z'_{\text{eff}} = \frac{a_{11} a_{22} - a_{12}^2}{a_{22}}, \quad (5)$$

$$\hat{\mu}_e = \frac{A_{11} A_{22} - A_{12}^2}{A_{22} Z'_{\text{eff}}}, \quad (6)$$

$$a_{11} = Z_{\text{eff}}, \quad (7)$$

$$a_{12} = \frac{3}{2} Z_{\text{eff}}, \quad (8)$$

$$a_{22} = \sqrt{2} + \frac{13}{4} Z_{\text{eff}}, \quad (9)$$

$$A_{11} = a_{11} + g_t (0.533 + Z_{\text{eff}}), \quad (10)$$

$$A_{12} = a_{12} + g_t \left(0.625 + \frac{3}{2} Z_{\text{eff}} \right), \quad (11)$$

$$A_{22} = a_{22} + g_t \left(1.386 + \frac{13}{4} Z_{\text{eff}} \right), \quad (12)$$

$$g_t = \frac{f_t}{1 - f_t}, \quad (13)$$

$$f_t(r) = \left[\tanh\left(\frac{r}{r_0}\right) \right]^{3/2} \left[1.46 \left(\frac{r}{R_0}\right)^{1/2} - 0.46 \left(\frac{r}{R_0}\right)^{3/2} \right]. \quad (14)$$

Here, m_e is the electron mass, e is the magnitude of the electron charge, $\ln \Lambda$ is the Coulomb logarithm, Z_{eff} is the effective ion charge number, and $f_t(r)$ is the fraction of trapped particles. Furthermore, $0 < r_0 \ll a$. Note that Z'_{eff} is the factor by which the plasma electrical conductivity is reduced due to the presence of impurity ions in the plasma, whereas $\hat{\mu}_e$ is the additional factor by which the conductivity is reduced due to the presence of trapped electrons.⁵¹ Note, further, that we have modified the expression for $f_t(r)$ in the immediate

vicinity of the magnetic axis (where it is not really valid anyway) in order to prevent the plasma current gradient from becoming singular in the limit $r \rightarrow 0$. Note, finally, that $\hat{\mu}_e \rightarrow 1$ as $r \rightarrow 0$.

Let $\hat{r} = r/a$. Suppose that

$$T_e(\hat{r}) = T_{e0} \hat{T}_e(\hat{r}), \quad (15)$$

where $\hat{T}_e(0) = 1$,

$$\hat{T}_e(1) = \zeta_e, \quad (16)$$

and $\hat{T}_e(\hat{r} > 1) = 0$. Here, T_{e0} is the central electron temperature and ζ_e is an assumed fixed ratio of the edge to the central electron temperature. It follows from Eqs. (2)–(4) and (15) that

$$\frac{1}{\hat{r}} \frac{d}{d\hat{r}} \left(\hat{r} \frac{d\hat{T}_e}{d\hat{r}} \right) = -\lambda_e \hat{T}_e^{3/2}(\hat{r}) \hat{\mu}_e^{-1}(\hat{r}), \quad (17)$$

for $0 \leq \hat{r} \leq 1$, and

$$\lambda_e = 1.13 \times 10^3 \frac{a^2 \bar{T}_{e0}^{1/2} E_{\parallel}^2}{\bar{\Lambda} Z'_{\text{eff}} \chi_E \bar{n}_e}, \quad (18)$$

where $\bar{n}_e = n_e/(10^{20})$, $\bar{T}_{e0} = T_{e0}/(10^3 \text{ e})$, and⁴⁸

$$\bar{\Lambda} = \frac{\ln \Lambda}{17} = \frac{14.8 - 0.5 \ln \bar{n}_e + \ln \bar{T}_{e0}}{17}. \quad (19)$$

D. Ohmic current density

The Ohmic toroidal current density in the plasma is given by^{47,48}

$$j_{\text{oh}} = \sigma_{\parallel} E_{\parallel}. \quad (20)$$

It follows from Eqs. (3), (4), and (15) that

$$j_{\text{oh}}(\hat{r}) = j_{\text{oh}0} \hat{j}_{\text{oh}}(\hat{r}), \quad (21)$$

where $j_{\text{oh}0}$ is the central toroidal current density, and

$$\hat{j}_{\text{oh}}(\hat{r}) = \hat{T}_e^{3/2}(\hat{r}) \hat{\mu}_e^{-1}(\hat{r}). \quad (22)$$

Note that $\hat{j}_{\text{oh}}(0) = 1$. It is easily demonstrated that

$$\bar{j}_{\text{oh}0} = 1.80 \times 10^1 \frac{\bar{T}_{e0}^{3/2} E_{\parallel}}{\bar{\Lambda} Z'_{\text{eff}}}, \quad (23)$$

where $\bar{j}_{\text{oh}0} = j_{\text{oh}0}/10^6$.

E. Bootstrap current density

The electron bootstrap current density is given by^{31,32}

$$j_{\text{bs}} = -\frac{n_e}{B_{\theta}} \frac{dT_e}{dr} f_{\text{bs}}, \quad (24)$$

where

$$f_{\text{bs}}(\hat{r}) = \frac{(A_{11} - a_{11} + a_{12}) A_{22} - (A_{12} - a_{12} + a_{22}) A_{12}}{A_{11} A_{22} - A_{12}^2}. \quad (25)$$

Note that $f_{\text{bs}} \rightarrow 0$ as $\hat{r} \rightarrow 0$, which ensures that $j_{\text{bs}} \rightarrow 0$ as $\hat{r} \rightarrow 0$ [because the ratio $(dT_e/dr)/B_{\theta}$ attains a constant value as $\hat{r} \rightarrow 0$].

F. Safety-factor profile

We can write

$$\frac{1}{r} \frac{d}{dr} (r B_\theta) = \mu_0 (j_{\text{oh}} + j_{\text{bs}}), \quad (26)$$

where

$$q(r) = \frac{r B_\phi f_a}{R_0 B_\theta} \quad (27)$$

is the safety-factor profile. Here,

$$f_a = \lambda_f \left[\frac{1 + \kappa_a^2 (1 + 2 \delta_a^2 - 1.22 \delta_a^3)}{2} \right] \left[\frac{1.17 - 0.65 \epsilon_a}{(1 - \epsilon_a^2)^2} \right], \quad (28)$$

where κ_a and δ_a are the vertical elongation and triangularity of the plasma boundary, respectively, whereas $\epsilon_a = a/R_0$ is the inverse aspect-ratio of the plasma boundary. The factor f_a is a correction to the conventional cylindrical expression for the safety-factor that takes plasma shaping and toroidicity into account.^{33,34} The adjustable parameter λ_f is used to obtain the desired plasma current (see Sec. VIB). Given that $j_{\text{oh}}(0) = j_{\text{oh}0}$ and $j_{\text{bs}}(0) = 0$, it follows from Eqs. (26) and (27) that

$$q_0 = \frac{5 B_\phi f_a}{\pi j_{\text{oh}0} R_0}, \quad (29)$$

where $q_0 = q(0)$ is the central safety-factor value.

Let

$$q(\hat{r}) = q_0 \hat{q}(\hat{r}). \quad (30)$$

According to Eqs. (15), (21), (24), and (26)–(29),

$$\frac{df}{d\hat{r}} = 2 \hat{r} \hat{j}_{\text{oh}}(\hat{r}) + 2 \beta_{\text{th}0} g_{\text{bs}}(\hat{r}) \frac{\hat{r}^2}{f}, \quad (31)$$

where

$$f(\hat{r}) = \frac{\hat{r}^2}{\hat{q}}, \quad (32)$$

$$\beta_{\text{th}0} = 1.01 \times 10^{-2} \left(\frac{\bar{n}_e \bar{T}_{e0}}{B_\phi^2 f_a^2} \right) \left(\frac{R_0 q_0}{a} \right)^2, \quad (33)$$

$$g_{\text{bs}}(\hat{r}) = - \frac{d\hat{T}_e}{d\hat{r}} f_{\text{bs}}(\hat{r}). \quad (34)$$

Note that $f \rightarrow \hat{r}^2$ as $\hat{r} \rightarrow 0$.

G. Power balance

The total thermal energy of the electrons is

$$W_e = 4\pi^2 R_0 \int_0^a \frac{3}{2} n_e T_e(r) r dr, \quad (35)$$

whereas the total electron energy loss rate is

$$P_e = -4\pi^2 a R_0 n_e \chi_E \frac{dT_e(a)}{dr}. \quad (36)$$

By definition, the mean energy confinement time of the electrons is $\bar{\tau}_E = W_e/P_e$. Thus,

$$\bar{\tau}_E = \frac{\kappa_e a^2}{\chi_E}, \quad (37)$$

where

$$\kappa_e = \frac{3}{2} \int_0^1 \hat{T}_e(\hat{r}) \hat{r} d\hat{r} / \left[- \frac{d\hat{T}_e(1)}{d\hat{r}} \right]. \quad (38)$$

Finally, E_{\parallel} and χ_E can be eliminated between Eqs. (18), (23), (29), and (37) to give

$$\bar{T}_{e0} = 2.38 \left(\frac{\bar{\Lambda} Z'_{\text{eff}} f_a^2}{\lambda_e \kappa_e q_0^2} \right)^{2/5} \left(\frac{\bar{\tau}_E B_\phi^2}{\bar{n}_e R_0^2} \right)^{2/5}. \quad (39)$$

H. Toroidal plasma current

The total toroidal plasma current is

$$I_p(t) = \int_0^a (j_{\text{oh}} + j_{\text{bs}}) 2\pi r dr. \quad (40)$$

Thus,

$$\bar{I}_p = \frac{5 a^2 B_\phi f_a}{R_0 q_a}, \quad (41)$$

where $\bar{I}_p = I_p/10^6$, $q_a = q(a)$ is the edge safety-factor value, and use has been made of Eqs. (26) and (27).

I. Ohmic heating rate

In a quasi-steady-state, the plasma Ohmic heating rate is equal to the energy loss rate, P_e . It follows from Eqs. (36) and (37) that

$$\bar{P}_e = 6.33 \times 10^{-1} \frac{\xi_e \bar{n}_e R_0 a^2 \bar{T}_{e0}}{\bar{\tau}_E}, \quad (42)$$

where $\bar{P}_e = P_e/10^6$, and

$$\xi_e = \frac{3}{2} \int_0^1 \hat{T}_e(\hat{r}) \hat{r} d\hat{r}. \quad (43)$$

J. Energy confinement time

At low densities, an ohmically heated tokamak plasma lies in the so-called linear Ohmic confinement (LOC) regime in which its energy confinement time scales linearly with the electron number density according to the neo-Alcator scaling law^{35,36}

$$\bar{\tau}_E = 9.0 \times 10^{-2} q_a \bar{n}_e a R_0^2. \quad (44)$$

Combining this expression with Eq. (39), we obtain

$$\bar{T}_{e0} = 9.08 \times 10^{-1} \left(\frac{\bar{\Lambda} Z'_{\text{eff}} f_a^2}{\lambda_e \kappa_e q_0^2} \right)^{2/5} q_a^{2/5} a^{2/5} B_\phi^{4/5}. \quad (45)$$

Note that the central electron temperature is independent of the electron number density in the LOC regime.

At higher densities, the plasma enters the so-called saturated Ohmic confinement (SOC) regime in which the linear scaling of the confinement time with electron number density breaks down.³⁵ In this regime, the energy confinement time is well approximated by the ITER-89P L-mode scaling law,^{29,37}

$$\bar{\tau}_E = 4.8 \times 10^{-2} M^{0.5} \kappa_a^{0.5} \bar{n}_e^{0.1} R_0^{1.2} a^{0.3} B_\phi^{0.2} \bar{I}_p^{0.85} \bar{P}_e^{-0.5}, \quad (46)$$

where M is the majority ion mass number. Equations (39), (41), (42), and (46) yield

$$\bar{\tau}_E = 6.88 \times 10^{-2} \left(\frac{\bar{\Lambda} Z'_{\text{eff}} f_a^2}{\lambda_e \kappa_e q_0^2} \right)^{-2/7} \left(\frac{M \kappa_a}{\zeta_e} \right)^{5/7} \left(\frac{f_a}{q_a} \right)^{17/14} \times \bar{n}_e^{-2/7} R_0^{5/14} a^{10/7} B_\phi^{13/14}, \quad (47)$$

$$\bar{T}_{e0} = 8.17 \times 10^{-1} \left(\frac{\bar{\Lambda} Z'_{\text{eff}} f_a^2}{\lambda_e \kappa_e q_0^2} \right)^{2/7} \left(\frac{M \kappa_a}{\zeta_e} \right)^{2/7} \left(\frac{f_a}{q_a} \right)^{17/35} \times \bar{n}_e^{-18/35} R_0^{-23/35} a^{4/7} B_\phi^{41/35}. \quad (48)$$

Note that both the confinement time and the central electron temperature decrease with increasing electron number density in the SOC regime.

The plasma lies in the LOC regime when the energy confinement time specified in Eq. (44) is less than that specified in Eq. (47), in which case the energy confinement time and the central electron temperature are given by Eqs. (44) and (45), respectively. In the opposite case, the plasma lies in the SOC regime, and the energy confinement time and the central electron temperature are given by Eqs. (47) and (48), respectively. It is clear from a comparison of Eqs. (44) and (47) that the plasma lies in the LOC regime when $\bar{n}_e < \bar{n}_{e\text{crit}}$, where

$$\bar{n}_{e\text{crit}} = 8.11 \times 10^{-1} \left(\frac{\bar{\Lambda} Z'_{\text{eff}} f_a^2}{\lambda_e \kappa_e q_0^2} \right)^{-2/9} \left(\frac{M \kappa_a}{\zeta_e} \right)^{5/9} \left(\frac{f_a}{q_a} \right)^{17/18} \left(\frac{1}{q_a} \right)^{7/9} \times R_0^{-23/18} a^{1/3} B_\phi^{13/18}. \quad (49)$$

K. Plasma profiles

We can calculate the profiles of significant plasma quantities by first solving Eq. (17), to determine $\hat{T}_e(\hat{r})$, subject to the boundary conditions,

$$\hat{T}_e(\hat{r}) = 1 - \frac{\lambda_e}{4} \hat{r}^2, \quad (50)$$

$$\frac{d\hat{T}_e}{d\hat{r}} = -\frac{\lambda_e}{2} \hat{r}, \quad (51)$$

when $0 < \hat{r} \ll 1$, and adjusting λ_e such that Eq. (16) is satisfied. Next, we need to solve Eq. (31), to determine $f(\hat{r})$, subject to the boundary condition,

$$f(\hat{r}) = \hat{r}^2, \quad (52)$$

when $0 < \hat{r} \ll 1$.

The normalized electron temperature profile is specified by

$$\bar{T}_e(\hat{r}) = \bar{T}_{e0} \hat{T}_e(\hat{r}), \quad (53)$$

where $\bar{T}_e = T_e/(10^3 e)$. The safety-factor profile is given by Eq. (30), where

$$\hat{q}(\hat{r}) = \frac{\hat{r}^2}{f(\hat{r})}. \quad (54)$$

The energy diffusivity is

$$\chi_E = \frac{\kappa_e a^2}{\bar{\tau}_E}. \quad (55)$$

The plasma toroidal beta profile is $\beta = 2 \mu_0 p/B_\phi^2$. It follows that

$$\beta(\hat{r}) = \beta_0 \hat{T}_e(\hat{r}), \quad (56)$$

where

$$\beta_0 = 4.03 \times 10^{-2} \frac{(1 + I_i) \bar{n}_e \bar{T}_{ec}}{B_\phi^2}. \quad (57)$$

Here, β_0 is the central plasma beta.

The normalized Ohmic current density profile is given by

$$\bar{j}_{\text{oh}}(\hat{r}) = \bar{j}_{\text{oh0}} \hat{j}_{\text{oh}}(\hat{r}), \quad (58)$$

where $\bar{j}_{\text{oh}} = j_{\text{oh}}/10^6$. The normalized electron bootstrap current density profile takes the form

$$\bar{j}_{\text{bs}}(\hat{r}) = \beta_{00} \bar{j}_{\text{oh0}} \hat{j}_{\text{bs}}(\hat{r}), \quad (59)$$

where $\bar{j}_{\text{bs}} = j_{\text{bs}}/10^6$, and

$$\hat{j}_{\text{bs}}(\hat{r}) = -\frac{\hat{q}(\hat{r})}{\hat{r}} \frac{d\hat{T}_e}{d\hat{r}} f_{\text{bs}}(\hat{r}). \quad (60)$$

L. Resistive layer parameters

As has already been mentioned, a tokamak plasma subject to an error-field develops a current sheet in a thin resistive layer located at the rational magnetic flux-surface within the plasma where the error-field resonates with the equilibrium magnetic field.^{21,23,24} The profiles of the various parameters that govern the properties of the resistive layer are as follows.

The magnetic shear profile, $s = r (dq/dr)/q$, is

$$s(\hat{r}) = 2 \left[1 - \hat{q}(\hat{r}) \hat{j}_\phi(\hat{r}) \right], \quad (61)$$

where

$$\hat{j}_\phi(\hat{r}) = \hat{j}_{\text{oh}}(\hat{r}) + \beta_{00} \hat{j}_{\text{bs}}(\hat{r}). \quad (62)$$

The electron diamagnetic frequency profile is⁴⁸

$$\omega_{*e} = -\frac{n q}{r} \frac{1}{e n_e B_\phi} \frac{dp_e}{dr}, \quad (63)$$

where n is the toroidal mode number of the error-field. It follows that

$$\omega_{*e}(\hat{r}) = \omega_{*e0} \hat{\omega}_{*e}(\hat{r}), \quad (64)$$

where

$$\omega_{*e0} = 5.00 \times 10^2 \frac{n \lambda_e q_0 \bar{T}_{e0}}{a^2 B_\phi}, \quad (65)$$

$$\hat{\omega}_{*e}(\hat{r}) = -\frac{2}{\lambda_e} \frac{\hat{q}(\hat{r})}{\hat{r}} \frac{d\hat{T}_e}{d\hat{r}}. \quad (66)$$

Here, ω_{*e0} is the central electron diamagnetic frequency. Note that $\hat{\omega}_{*e}(0) = 1$.

The ion diamagnetic frequency profile is

$$\omega_{*i}(\hat{r}) = -l_i \omega_{*e0} \hat{\omega}_{*e}(\hat{r}). \quad (67)$$

The $\mathbf{E} \times \mathbf{B}$ frequency profile is

$$\omega_E(\hat{r}) = l_E \omega_{*e0} \hat{\omega}_{*e}(\hat{r}), \quad (68)$$

where l_E is an assumed spatially uniform ratio between the values of ω_E and ω_{*e} . Observations of intrinsic toroidal ion rotation in ohmically heated tokamak plasmas indicate that the rotation is roughly diamagnetic in magnitude, is in the co-current direction at low densities, and switches to the countercurrent at intermediate densities but switches back to the co-current direction at high densities.^{52,53} The low density to intermediate density rotation reversal is associated with the LOC to SOC transition.³⁷ These observations suggest that l_E is of order unity (corresponding to an $\mathbf{E} \times \mathbf{B}$ velocity that is of order a diamagnetic velocity) and is less than unity at low (LOC regime) densities and high densities but is greater than unity at intermediate (SOC regime) densities.

The hydromagnetic timescale profile is²⁴

$$\tau_H(\hat{r}) = \tau_{H0} \hat{\tau}_H(\hat{r}), \quad (69)$$

where

$$\tau_{H0} = \frac{R_0 \sqrt{\mu_0 n_e M m_p}}{n B_\phi} = 4.58 \times 10^{-7} \frac{R_0 \sqrt{M n_e}}{n B_\phi}, \quad (70)$$

$$\hat{\tau}_H(\hat{r}) = \frac{1}{s(\hat{r})}. \quad (71)$$

Here, m_p is the proton mass.

The resistive evolution timescale profile is $\tau_R = \mu_0 r^2 \sigma_{||}$. It follows from Eqs. (3) and (4) that

$$\tau_R(\hat{r}) = \tau_{R0} \hat{\tau}_R(\hat{r}), \quad (72)$$

where

$$\tau_{R0} = 2.27 \times 10^1 \frac{a^2 \bar{T}_{e0}^{3/2}}{\Lambda Z'_{\text{eff}}}, \quad (73)$$

$$\hat{\tau}_R(\hat{r}) = \hat{r}^2 \hat{j}_{\text{oh}}(\hat{r}). \quad (74)$$

The Lundquist number profile is $S = \tau_R/\tau_H$. It follows that

$$S(\hat{r}) = S_0 \hat{S}(\hat{r}), \quad (75)$$

where

$$S_0 = \frac{\tau_{R0}}{\tau_{H0}}, \quad (76)$$

$$\hat{S}(\hat{r}) = \hat{r}^2 \hat{j}_{\text{oh}}(\hat{r}) s(\hat{r}). \quad (77)$$

The ion sound radius profile is $d_\beta = [(5/6) m_i \beta / (n_e e^2 \mu_0)]^{1/2}$.²⁴ It follows that

$$d_\beta(\hat{r}) = d_{\beta 0} \hat{d}_\beta(\hat{r}), \quad (78)$$

where

$$d_{\beta 0} = 2.95 \times 10^{-3} \left[\frac{(1 + l_i) M \bar{T}_{e0}}{B_\phi^2} \right]^{1/2}, \quad (79)$$

$$\hat{d}_\beta(\hat{r}) = \hat{T}_e^{1/2}(\hat{r}). \quad (80)$$

Finally, the energy confinement time profile is $\tau_E = r^2/\chi_E$. It follows that

$$\tau_E(\hat{r}) = \tau_{E0} \hat{\tau}_E(\hat{r}), \quad (81)$$

where

$$\tau_{E0} = \frac{a^2}{\chi_E}, \quad (82)$$

$$\hat{\tau}_E(\hat{r}) = \hat{r}^2. \quad (83)$$

III. OUTER REGION

A. Introduction

The aim of this section is to describe the plasma response to the error-field in the outer region.

B. Cylindrical tearing mode equation

The perturbed magnetic flux associated with the plasma response can be written as²¹

$$\delta\psi(r, \theta, \varphi) = \psi(r) e^{i(m\theta - n\varphi)}. \quad (84)$$

The associated perturbed magnetic field is²¹

$$\delta B_r = i \frac{m}{r} \delta\psi, \quad (85)$$

$$\delta B_\theta = -\frac{d\delta\psi}{dr}, \quad (86)$$

$$\delta B_\varphi \simeq 0. \quad (87)$$

The function $\psi(r)$ satisfies the cylindrical tearing mode equation,²¹

$$\frac{d^2\psi}{d\hat{r}^2} + \frac{1}{\hat{r}} \frac{d\psi}{d\hat{r}} - \frac{m^2}{\hat{r}^2} \psi - \frac{J' \psi}{\hat{r} (1/q - n/m)} = 0, \quad (88)$$

where

$$J'(\hat{r}) = \frac{dJ}{d\hat{r}}, \quad (89)$$

$$J(\hat{r}) = \frac{R_0 \mu_0 (j_{\text{oh}} + j_{\text{bs}})}{B_\phi f_a}. \quad (90)$$

It follows from Eqs. (29) and (58)–(60) that

$$J(\hat{r}) = \frac{2}{q_0} \left[\hat{j}_{\text{oh}}(\hat{r}) + \beta_{00} \hat{j}_{\text{bs}}(\hat{r}) \right] \quad (91)$$

for $0 \leq \hat{r} \leq 1$ and $J(\hat{r}) = 0$ for $\hat{r} > 1$. Note that Eq. (88) is singular at the rational surface, of normalized minor radius \hat{r}_s , at which $q(\hat{r}_s) = m/n$. The singularity is indicative of the breakdown of the equations of linearized, marginally stable, ideal MHD in the inner region.

C. Solution of cylindrical tearing mode equation

Suppose that the plasma is surrounded by a perfectly conducting wall located at $r = b$, where $b > a$. Let $\psi(b) = \Psi_b$, where Ψ_b is a complex constant that specifies the amplitude and phase of the error-field

to which the plasma is subject. The plasma response in the outer region is specified by

$$\psi(\hat{r}) = \Psi_s \hat{\psi}_s(\hat{r}) + \Psi_b \hat{\psi}_b(\hat{r}). \quad (92)$$

Here, $\hat{\psi}_s(\hat{r})$ is a real continuous solution of Eq. (88) that satisfies

$$\hat{\psi}_s(0) = 0, \quad (93)$$

$$\hat{\psi}_s(\hat{r}_s) = 1, \quad (94)$$

$$\left[\frac{\hat{r}}{\hat{\psi}_s} \frac{d\hat{\psi}_s}{d\hat{r}} \right]_{\hat{r}=1-}^{\hat{r}=1+} = -\frac{J(1)}{[1/q(1) - n/m]}, \quad (95)$$

$$\hat{\psi}_s(\hat{r} \geq \hat{b}) = 0, \quad (96)$$

where $\hat{b} = b/a$. Moreover, $\hat{\psi}_b(\hat{r})$ is a real continuous solution of Eq. (88) that satisfies

$$\hat{\psi}_b(\hat{r} \leq \hat{r}_s) = 0, \quad (97)$$

$$\left[\frac{\hat{r}}{\hat{\psi}_b} \frac{d\hat{\psi}_b}{d\hat{r}} \right]_{\hat{r}=1-}^{\hat{r}=1+} = -\frac{J(1)}{[1/q(1) - n/m]}, \quad (98)$$

$$\hat{\psi}_b(\hat{b}) = 1. \quad (99)$$

Note that the complex quantity Ψ_s specifies the amplitude and phase of the reconnected magnetic flux driven at the rational surface by the error-field.

D. Calculation of $\hat{\psi}_s(\hat{r})$

In the limit $0 < \hat{r} \ll 1$, we have

$$\hat{\psi}_s(\hat{r}) \propto \hat{r}^m + \kappa_0 \hat{r}^{m+2}, \quad (100)$$

where

$$\kappa_0 = -\frac{x_0}{(m+1)(1 - q_0 n/m)}, \quad (101)$$

and $x_0 = \lim_{\hat{r} \rightarrow 0} [(1 - q_0 J/2)/\hat{r}^2]$.

Let $\rho = (\hat{r} - \hat{r}_s)/\hat{r}_s$. In the immediate vicinity of the rational surface,

$$\hat{\psi}_s(\rho) = 1 + \Delta_{s+} \rho + \alpha_s \rho \ln |\rho| + \mathcal{O}(\rho^2) \quad (102)$$

for $\rho > 0$, and

$$\hat{\psi}_s(\rho) = 1 + \Delta_{s-} \rho + \alpha_s \rho \ln |\rho| + \mathcal{O}(\rho^2) \quad (103)$$

for $\rho < 0$, where

$$\alpha_s = -\left(\frac{\hat{r} q J'}{s} \right)_{\hat{r}=\hat{r}_s}. \quad (104)$$

In particular,

$$\Delta_{s\pm} = \frac{\hat{r}}{\hat{\psi}_s} \frac{d\hat{\psi}_s}{d\hat{r}} - \alpha_s (1 + \ln |\rho|), \quad (105)$$

in the limit that $\rho \rightarrow 0_{\pm}$.

Finally,

$$\left(\frac{\hat{r}}{\hat{\psi}_s} \frac{d\hat{\psi}_s}{d\hat{r}} \right)_{\hat{r}=1-} = -m \left(\frac{\hat{b}^{2m} + 1}{\hat{b}^{2m} - 1} \right) + \frac{J(1)}{[1/q(1) - n/m]}. \quad (106)$$

We can calculate $\hat{\psi}_s(\hat{r})$ by first launching a solution of Eq. (88) from the magnetic axis, subject to the boundary condition (100), and integrating to just inside the rational surface. Next, we launch a second solution of Eq. (88) from just inside the plasma boundary, subject to the boundary condition (106), and integrate to just outside the rational surface. The two solutions are then rescaled subject to the constraint $\hat{\psi}_s(\hat{r}_s) = 1$. Finally, the parameters $\Delta_{s\pm}$ are determined using Eq. (105). The real quantity

$$E_{ss} \equiv \left[\hat{r} \frac{d\hat{\psi}_s}{d\hat{r}} \right]_{\hat{r}=\hat{r}_{s-}}^{\hat{r}=\hat{r}_{s+}} = \Delta_{s+} - \Delta_{s-} \quad (107)$$

is the conventional tearing stability index.⁵⁴

E. Calculation of $\hat{\psi}_b(\hat{r})$

In order to calculate $\hat{\psi}_b(\hat{r})$, we launch a solution of Eq. (88) from just outside the rational surface, such that

$$\hat{\psi}_b(\hat{r}_s) = 0, \quad (108)$$

$$\frac{d\hat{\psi}_b(\hat{r}_s)}{d\hat{r}} = \frac{1}{\hat{r}_s}, \quad (109)$$

and then integrate it to just inside the plasma boundary. Let

$$\alpha_b = \frac{1}{2m} \left[m \hat{b}^m \hat{\psi}_b(1) + \hat{b}^m \frac{d\hat{\psi}_b(1)}{d\hat{r}} \right], \quad (110)$$

$$\beta_b = \frac{1}{2m} \left[m \hat{b}^{-m} \hat{\psi}_b(1) - \hat{b}^{-m} \frac{d\hat{\psi}_b(1)}{d\hat{r}} \right], \quad (111)$$

$$\gamma_b = \frac{J(1)}{2m} \frac{\hat{b}^m - \hat{b}^{-m}}{[1/q(1) - n/m]}, \quad (112)$$

$$\delta_b = \alpha_b + \beta_b - \gamma_b (\alpha_b \hat{b}^{-m} + \beta_b \hat{b}^m). \quad (113)$$

The boundary condition (99) is satisfied by dividing our solution by δ_b .

If we define the real quantity

$$E_{sb} = \left[\hat{r} \frac{d\hat{\psi}_b}{d\hat{r}} \right]_{\hat{r}=\hat{r}_{s+}}, \quad (114)$$

then it follows that $E_{sb} = 1/\delta_b$.

F. Asymptotic matching

Asymptotic matching between the solution of Eq. (88) in the outer region and the thin resistive layer, centered on the rational surface, that constitutes the inner region yields²¹

$$\Delta_s \Psi_s = E_{ss} \Psi_s + E_{sb} \Psi_b, \quad (115)$$

where use has been made of Eqs. (92), (107), and (114). Here, the complex quantity Δ_s specifies the magnitude and phase of the shielding current that is generated in the inner region. In the presence of the shielding current, the amount of reconnected flux driven at the rational surface is

$$\frac{\Psi_s}{\Psi_b} = \frac{E_{sb}}{\Delta_s - E_{ss}}. \quad (116)$$

On the other hand, in the absence of the shielding current, the driven magnetic flux is given by

$$\frac{\Psi_s}{\Psi_b} = \frac{E_{sb}}{-E_{ss}}. \quad (117)$$

Hence, the shielding factor (i.e., the ratio of the magnitudes of the reconnected fluxes in the absence and in the presence of the shielding current) is

$$\Sigma = \frac{|\Delta_s - E_{ss}|}{(-E_{ss})}. \quad (118)$$

Let

$$\Psi_b = R_0 B_\phi \hat{\Psi}_b. \quad (119)$$

The unshielded radial magnetic field at the rational surface, due to the error-field, is

$$\frac{b_v}{B_\phi} = \frac{m R_0}{\hat{r}_s a} \frac{E_{sb}}{(-E_{ss})} |\hat{\Psi}_b|. \quad (120)$$

G. Electromagnetic torques

The flux-surface integrated poloidal and toroidal electromagnetic torques exerted on the plasma by the external magnetic perturbation are²¹

$$T_\theta(r) = T_{\theta s} \delta(r - r_s), \quad (121)$$

$$T_\varphi(r) = T_{\varphi s} \delta(r - r_s), \quad (122)$$

where

$$T_{\theta s} = -\frac{2\pi^2 R_0 m}{\mu_0} \text{Im}(\Delta_s |\Psi_s|^2), \quad (123)$$

$$T_{\varphi s} = \frac{2\pi^2 R_0 n}{\mu_0} \text{Im}(\Delta_s |\Psi_s|^2). \quad (124)$$

It follows that

$$T_{\theta s} = -\frac{2\pi^2 R_0^3 B_\phi^2}{\mu_0} m |\hat{\Psi}_b|^2 \frac{E_{sb}^2 \text{Im}(\Delta_s)}{|\Delta_s - E_{ss}|^2}, \quad (125)$$

$$T_{\varphi s} = \frac{2\pi^2 R_0^3 B_\phi^2}{\mu_0} n |\hat{\Psi}_b|^2 \frac{E_{sb}^2 \text{Im}(\Delta_s)}{|\Delta_s - E_{ss}|^2}, \quad (126)$$

where use has been made of Eqs. (116) and (119). Note that $T_{\theta s} = -(m/n) T_{\varphi s}$.²¹

IV. INNER REGION

A. Introduction

The resistive layer that constitutes the inner region is assumed to be governed by the linearized two-fluid model described in Ref. 24. This model is an extension of a model introduced in Ref. 23 and is ultimately based on the four-field equations of Hazeltine *et al.*³⁸

B. Layer parameters

According to our model, the parameters that control the response of the resistive layer are

$$Q_e = \hat{r}^{2/3} S^{1/3} \omega_{*e} \tau_H, \quad (127)$$

$$Q_i = \hat{r}^{2/3} S^{1/3} \omega_{*i} \tau_H, \quad (128)$$

$$Q_E = \hat{r}^{2/3} S^{1/3} \omega_E \tau_H, \quad (129)$$

$$D = \hat{r}^{-1/3} S^{1/3} \left(\frac{1}{1 + I_i} \right)^{1/2} \frac{d_\beta}{r}, \quad (130)$$

$$P_\perp = P_\varphi = \frac{\tau_R}{\tau_E}. \quad (131)$$

Note that we are equating the energy confinement and momentum confinement timescales for the sake of simplicity.

Making use of the results of Secs. II K and III L, we obtain

$$Q_e(\hat{r}) = Q_{e0} \hat{Q}_e(\hat{r}), \quad (132)$$

where

$$Q_{e0} = S_0^{1/3} \omega_{e0} \tau_{H0}, \quad (133)$$

$$\hat{Q}_e(\hat{r}) = \left[\frac{\hat{r}^4 \hat{j}_{\text{oh}}(\hat{r})}{s^2(\hat{r})} \right]^{1/3} \hat{\omega}_e(\hat{r}). \quad (134)$$

Furthermore,

$$Q_i(\hat{r}) = -I_i Q_e(\hat{r}), \quad (135)$$

$$Q_E(\hat{r}) = I_E Q_e(\hat{r}). \quad (136)$$

We also have

$$D(\hat{r}) = D_0 \hat{D}(\hat{r}), \quad (137)$$

where

$$D_0 = \left(\frac{1}{1 + I_i} \right)^{1/2} \frac{S_0^{1/3} d_{\beta 0}}{a}, \quad (138)$$

$$\hat{D}(\hat{r}) = \left[\frac{s(\hat{r}) \hat{j}_{\text{oh}}(\hat{r})}{\hat{r}^2} \right]^{1/3} \hat{d}_\beta(\hat{r}). \quad (139)$$

Finally,

$$P_\perp(\hat{r}) = P_{\perp 0} \hat{P}_\perp(\hat{r}), \quad (140)$$

where

$$P_{\perp 0} = \frac{\tau_{R0}}{\tau_{E0}}, \quad (141)$$

$$\hat{P}_\perp(\hat{r}) = \hat{j}_{\text{oh}}(\hat{r}), \quad (142)$$

and

$$P_\varphi(\hat{r}) = P_\perp(\hat{r}). \quad (143)$$

C. Calculation of Δ_s

The layer response index is

$$\Delta(\hat{r}) = \hat{r} S_*^{1/3}(\hat{r}) \hat{\Delta}(\hat{r}), \quad (144)$$

where

$$Y_e(p) \rightarrow Y_0 \left[\frac{\hat{\Delta}}{\pi p} + 1 + \mathcal{O}(p) \right], \quad (145)$$

as $p \rightarrow 0$, and $Y_e(p)$ is the solution that is bounded as $p \rightarrow \infty$ of²⁴

$$\frac{d}{dp} \left[A(p) \frac{dY_e}{dp} \right] - \frac{B(p)}{C(p) \hat{r}^2} p^2 Y_e = 0, \quad (146)$$

with

$$A(p) = \frac{p^2}{-i(-Q_E - Q_e) + p^2}, \quad (147)$$

$$B(p) = -(-Q_E)(-Q_E - Q_i) - i(-Q_E - Q_i)(P_\phi + P_\perp) p^2 + P_\phi P_\perp p^4, \quad (148)$$

$$C(p) = -i(-Q_E - Q_i) + [P_\perp - i(-Q_E - Q_i) D^2] p^2 + (1 + i_t) P_\phi D^2 p^4. \quad (149)$$

Furthermore, $S_* = \hat{r}^{-4} S$. It follows that

$$S_*^{1/3}(\hat{r}) = S_0^{1/3} \hat{S}_*^{1/3}(\hat{r}), \quad (150)$$

$$\hat{S}_*^{1/3}(\hat{r}) = \left[\frac{s(\hat{r}) \hat{j}_{\text{oh}}(\hat{r})}{\hat{r}^2} \right]^{1/3}. \quad (151)$$

Finally,

$$\Delta_s = \Delta(\hat{r}_s). \quad (152)$$

The most convenient method of solving Eq. (146) is by means of a Riccati transformation.^{55,56}

V. TORQUE BALANCE

A. Introduction

The electromagnetic torque exerted at the rational surface by the error-field acts to arrest the rotation of the local electron fluid, thereby (in most cases) eliminating the shielding current.²¹ This action is opposed by viscous torques that develop at the rational surface. As described in this section, the rotation of the electron fluid at the rational surface is determined by balancing the electromagnetic and viscous torques.

B. Plasma poloidal angular equation of motion

The plasma poloidal equation of angular motion is written as²¹

$$-4\pi^2 R_0 \left[\frac{d}{dr} \left(\rho \Xi_\perp r^3 \frac{d\Delta\Omega_\theta}{dr} \right) - \frac{\rho}{\tau_\theta} r^3 \Delta\Omega_\theta \right] = T_{\theta s} \delta(r - r_s), \quad (153)$$

where $\Delta\Omega_\theta(r)$ is the change in the plasma poloidal angular velocity profile induced by the electromagnetic torque that develops at the rational surface, $\rho = n_e M m_p$ is the plasma mass density, and $\Xi_\perp = \chi_E$ is the plasma toroidal momentum diffusivity. Moreover,^{32,50}

$$\tau_\theta = \frac{r^2}{q^2 R_0^2} \frac{\tau_i}{g_t \hat{\mu}_i}, \quad (154)$$

$$\tau_i = \frac{6\sqrt{2} \pi^{3/2} \epsilon_0^2 M^{1/2} m_p^{1/2} i_i^{3/2} T_e^{3/2}}{\ln \Lambda e^4 n_e}, \quad (155)$$

$$\hat{\mu}_i = 0.533 + \alpha_I, \quad (156)$$

$$\alpha_I = \frac{Z_I (Z_{\text{eff}} - 1)}{Z_I - Z_{\text{eff}}}. \quad (157)$$

Here, τ_θ is the neoclassical poloidal flow-damping time, and Z_I is the impurity ion charge number. Equation (153) must be solved subject to the boundary conditions,²¹

$$\frac{d\Delta\Omega_\theta(0)}{dr} = 0, \quad (158)$$

$$\Delta\Omega_\theta(a) = 0. \quad (159)$$

The modification of the $\mathbf{E} \times \mathbf{B}$ frequency induced by the change in the toroidal angular velocity profile is

$$\Delta\omega_{E\theta}(\hat{r}) = m \Delta\Omega_\theta(\hat{r}). \quad (160)$$

It follows from Eqs. (70), (82), (125), and (153) that

$$\begin{aligned} & \frac{d}{d\hat{r}} \left(\hat{r}^3 \frac{d\Delta\omega_{E\theta}}{d\hat{r}} \right) - \frac{\hat{r}^3 \Delta\omega_{E\theta}}{\lambda_\theta^2} \\ &= \frac{1}{2} \left(\frac{m}{n} \right)^2 \left(\frac{R_0}{a} \right)^4 \left(\frac{\tau_{E0}}{\tau_{H0}^2} \right) |\hat{\Psi}_b|^2 \frac{E_{sb}^2 \text{Im}(\Delta_s)}{|\Delta_s - E_{ss}|^2} \delta(\hat{r} - \hat{r}_s), \end{aligned} \quad (161)$$

which must be solved subject to the constraints

$$\frac{d\Delta\omega_{E\theta}(0)}{d\hat{r}} = 0, \quad (162)$$

$$\Delta\omega_{E\theta}(1) = 0. \quad (163)$$

Here,

$$\lambda_\theta = \left[\frac{\tau_\theta(\hat{r}_s)}{\tau_{E0}} \right]^{1/2}. \quad (164)$$

It follows that

$$\lambda_\theta = \lambda_{\theta 0} \hat{\lambda}_\theta(\hat{r}_s), \quad (165)$$

$$\lambda_{\theta 0} = 1.66 \times 10^{-2} \frac{n}{m} \frac{a}{R_0} \left(\frac{M^{1/2} i_i^{3/2} T_e^{3/2}}{\Lambda \hat{\mu}_i \bar{n}_e \tau_{E0}} \right)^{1/2}, \quad (166)$$

$$\hat{\lambda}_\theta(\hat{r}) = \left[\frac{\hat{r}^2 \hat{T}_e^{3/2}(\hat{r})}{g_t(\hat{r})} \right]^{1/2}. \quad (167)$$

Note that we have replaced $\lambda_\theta(\hat{r})$ by $\lambda_\theta(\hat{r}_s)$ in Eq. (161) because $\lambda_\theta(\hat{r}_s)$ is usually very much less than unity, which implies that $\Delta\omega_{E\theta}(\hat{r})$ is usually strongly localized in the vicinity of the rational surface. This localization causes $\Delta\omega_{E\theta}(\hat{r})$ to be much less than $\Delta\omega_{E\phi}(\hat{r})$ [see Eq. (173)]. In other words, as a consequence of strong poloidal flow-damping, the modification of the $\mathbf{E} \times \mathbf{B}$ frequency induced by the change in the poloidal angular velocity profile is usually much less than that induced by the change in the toroidal angular velocity profile. However, at very low plasma densities, $\lambda_\theta(\hat{r}_s)$ ceases to be much less than unity, which means that we need to include $\Delta\omega_{E\theta}(\hat{r})$ in the calculation.

It is easily demonstrated that

$$\Delta\omega_{E\theta}(\hat{r}_s) = -\frac{1}{2} \left(\frac{m}{n} \right)^2 \left(\frac{R_0}{a} \right)^4 \left(\frac{\tau_{E0}}{\tau_{H0}^2} \right) |\hat{\Psi}_b|^2 \frac{E_{sb}^2 \text{Im}(\Delta_s)}{|\Delta_s - E_{ss}|^2} F_\theta, \quad (168)$$

where

$$F_\theta = \frac{I_1(\hat{r}_s/\lambda_\theta)}{\hat{r}_s^2 I_1(1/\lambda_\theta)} [I_1(1/\lambda_\theta) K_1(\hat{r}_s/\lambda_\theta) - I_1(\hat{r}_s/\lambda_\theta) K_1(1/\lambda_\theta)] \simeq \frac{\lambda_\theta}{2 \hat{r}_s^3}. \quad (169)$$

Here, $I_1(x)$ and $K_1(x)$ are Bessel functions.

C. Plasma toroidal angular equation of motion

The plasma toroidal equation of angular motion is written as²¹

$$-4\pi^2 R_0^3 \frac{d}{dr} \left(\rho \Xi_{\perp} r \frac{d\Delta\Omega_{\phi}}{dr} \right) = T_{\phi s} \delta(r - r_s), \quad (170)$$

where $\Delta\Omega_{\phi}(r)$ is the change in the plasma toroidal angular velocity profile induced by the electromagnetic torque that develops at the rational surface. The previous equation must be solved subject to the boundary conditions,²¹

$$\frac{d\Delta\Omega_{\phi}(0)}{dr} = 0, \quad (171)$$

$$\Delta\Omega_{\phi}(a) = 0. \quad (172)$$

The modification of the $\mathbf{E} \times \mathbf{B}$ frequency induced by the change in the toroidal angular velocity profile is

$$\Delta\omega_{E\phi}(\hat{r}) = -n \Delta\Omega_{\phi}(\hat{r}). \quad (173)$$

It follows from Eqs. (70), (82), (126), and (170) that

$$\frac{d}{d\hat{r}} \left(\hat{r} \frac{d\Delta\omega_{E\phi}}{d\hat{r}} \right) = \frac{1}{2} \left(\frac{R_0}{a} \right)^2 \left(\frac{\tau_{E0}}{\tau_{H0}^2} \right) |\hat{\Psi}_b|^2 \frac{E_{sb}^2 \text{Im}(\Delta_s)}{|\Delta_s - E_{ss}|^2} \delta(\hat{r} - \hat{r}_s), \quad (174)$$

which must be solved subject to the constraints

$$\frac{d\Delta\omega_{E\phi}(0)}{d\hat{r}} = 0, \quad (175)$$

$$\Delta\omega_{E\phi}(1) = 0. \quad (176)$$

It is easily demonstrated that

$$\Delta\omega_{E\phi}(\hat{r}_s) = -\frac{1}{2} \left(\frac{R_0}{a} \right)^2 \left(\frac{\tau_{E0}}{\tau_{H0}^2} \right) |\hat{\Psi}_b|^2 \frac{E_{sb}^2 \text{Im}(\Delta_s)}{|\Delta_s - E_{ss}|^2} \ln \left(\frac{1}{\hat{r}_s} \right). \quad (177)$$

D. Torque balance equation

Equations (70), (71), (76), (77), (68), (168), and (177) yield the normalized torque balance equation,

$$Q_E(\hat{r}_s) = \iota_E Q_e(\hat{r}_s) - T_{\theta 0} \hat{T}_{\theta}(\hat{r}_s) - T_{\phi 0} \hat{T}_{\phi}(\hat{r}_s), \quad (178)$$

where

$$T_{\theta 0} = \frac{1}{2} \left(\frac{m}{n} \right)^2 \left(\frac{R_0}{a} \right)^4 \left(\frac{\tau_{E0}}{\tau_{H0}} \right) S_0^{1/3} |\hat{\Psi}_b|^2, \quad (179)$$

$$\hat{T}_{\theta}(\hat{r}_s) = \left[\frac{\hat{r}_s^4 \hat{j}_{\text{oh}}(\hat{r}_s)}{s^2(\hat{r}_s)} \right]^{1/3} F_{\theta} \frac{E_{sb}^2 \text{Im}(\Delta_s)}{|\Delta_s - E_{ss}|^2}, \quad (180)$$

and

$$T_{\phi 0} = \frac{1}{2} \left(\frac{R_0}{a} \right)^2 \left(\frac{\tau_{E0}}{\tau_{H0}} \right) S_0^{1/3} |\hat{\Psi}_b|^2, \quad (181)$$

$$\hat{T}_{\phi}(\hat{r}_s) = \left[\frac{\hat{r}_s^4 \hat{j}_{\text{oh}}(\hat{r}_s)}{s^2(\hat{r}_s)} \right]^{1/3} \ln \left(\frac{1}{\hat{r}_s} \right) \frac{E_{sb}^2 \text{Im}(\Delta_s)}{|\Delta_s - E_{ss}|^2}. \quad (182)$$

VI. RESULTS

A. Machine parameters

Table I lists the machine parameters for ITER and SPARC plasmas that are used as inputs to our calculation. Most of these parameters are taken from Refs. 25 and 26. We are assuming that the majority ion species is deuterium (i.e., $M = 2$), and that the impurity ion species is carbon (i.e., $Z_I = 6$) (note that our calculation exhibits very little sensitivity to the impurity ion charge number). We are also assuming that the electrons and the majority ions have the same temperature (i.e., $\iota_i = 1$). This assumption is reasonable because, in both machines, the ion-electron energy equilibration time is about 0.25 s, which is significantly less than the energy confinement time (see Table II). The assumed ratio of the edge to the central electron temperature is $\zeta_e = 10^{-3}$. Finally, the near-axis trapped particle regularization radius is $r_0 = 0.05 a$.

B. Plasma parameters

The data shown in Table I, used in combination with the analysis of Sec. II, yield the estimated plasma parameters characterizing ITER and SPARC ohmically heated plasmas that are shown in Table II. The central safety-factor, q_0 , and the parameter λ_f [see Eq. (28)] have both been adjusted to obtain the desired edge safety-factor and plasma current. The normalized temperature and current density profiles, as well as the safety-factor and magnetic shear profiles, for an ITER ohmically heated plasma are shown in Fig. 1 (the SPARC profiles are virtually identical).

In both machines, the critical electron number density above which the plasma lies in the SOC regime, rather than the LOC regime (see Sec. II J), is below the normal operating electron number density. This implies that, in normal circumstances, both ITER and SPARC ohmically heated plasmas lie in the SOC regime. It can be seen that

TABLE I. Assumed machine parameters for ITER and SPARC. Here, B_{ϕ} is the toroidal magnetic field-strength, R_0 is the major radius, a is the minor radius, I_p is the toroidal plasma current, n_e is the electron number density, κ_a is the boundary elongation, δ_a is the boundary triangularity, M is the majority ion mass number, Z_I is the impurity ion charge number, Z_{eff} is the effective ion charge number, ι_i is the ratio of the ion to the electron temperature, q_a is the edge safety-factor, and b is the wall radius.

Machine	ITER	SPARC
B_{ϕ} (T)	5.3	12.2
R_0 (m)	6.2	1.85
a (m)	2.0	0.57
I_p (MA)	15.0	8.7
n_e (10^{20} m^{-3})	1.0	3.0
κ_a	1.8	1.97
δ_a	0.4	0.54
M	2	2
Z_I	6	6
Z_{eff}	2.0	2.0
ι_i	1.0	1.0
q_a	3.2	3.2
b/a	1.2	1.2

TABLE II. Estimated plasma parameters in ITER and SPARC ohmically heated plasmas. The dimensionless electron temperature profile parameters λ_e , λ_f , κ_e , and ζ_e are defined in Eqs. (18), (28), (38), and (43), respectively. n_{ecrit} is the critical electron number density above which the plasma enters the SOC regime, T_{e0} is the central electron temperature, P_e is the Ohmic heating power, $\bar{\tau}_E$ is the mean energy confinement time, β_0 is the central toroidal beta, β_{00} is the central poloidal beta, and q_0 is the central safety-factor.

Machine	ITER	SPARC
λ_f	0.54	0.40
λ_e	13.8	13.5
κ_e	0.31	0.31
ζ_e	0.27	0.27
$n_{\text{ecrit}}(10^{20} \text{ m}^{-3})$	0.30	1.8
$T_{e0}(\text{keV})$	9.7	14.7
$P_e(\text{MW})$	8.4	5.4
$\bar{\tau}_E(\text{s})$	4.8	0.84
β_0	2.8×10^{-2}	2.4×10^{-2}
β_{00}	7.2×10^{-4}	8.5×10^{-4}
q_0	0.42	0.43

Ohmic heating in ITER gives rise to a plasma with a central electron temperature of about 9.7 keV, whereas Ohmic heating in SPARC gives rise to a central electron temperature of about 14.7 keV. In both machines, the toroidal beta is about 2.5%, but the poloidal beta is very small. Finally, in both machines, the central safety-factor is about 0.42.

The reason that we have had to adopt an unrealistically low value of the central safety-factor in order to get a realistic edge safety-factor is evident from Fig. 1. It can be seen from the figure that, although the electron temperature profile is quite broad, the current density profile is strongly peaked. The strong peaking of the current density profile is a direct consequence of the neoclassical reduction in the electrical conductivity of the plasma consequent on the existence of trapped electrons (incidentally, given the estimated electron temperatures, it is clear that the plasmas in both machines are in the banana collisionality regime). In fact, the factor by which the conductivity is multiplied in the presence of trapped electrons, $\hat{\mu}_e^{-1}$ (see Sec. II C), is shown in the

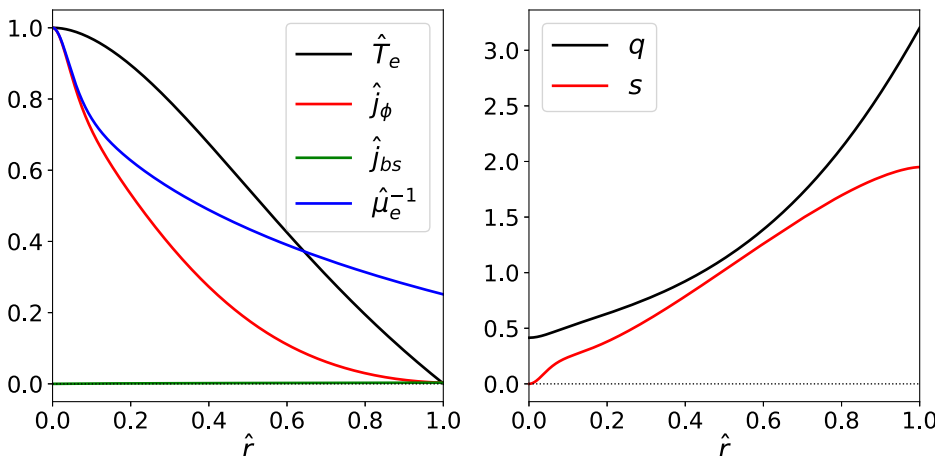


FIG. 1. Equilibrium profiles in an ITER ohmically heated plasma. Here, \hat{r} is the normalized minor radius, \hat{T}_e is the normalized electron temperature, \hat{j}_ϕ is the normalized toroidal current density, \hat{j}_{bs} is the normalized bootstrap current density, $\hat{\mu}_e^{-1}$ is the factor by which the plasma electrical resistivity is multiplied in the presence of trapped electrons, q is the safety-factor, and s is the magnetic shear.

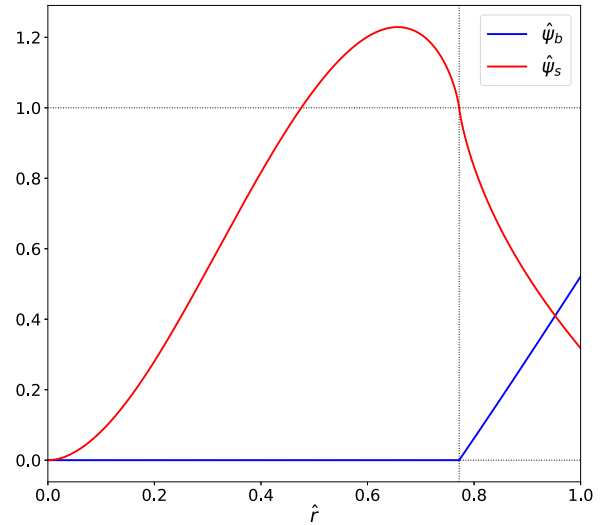


FIG. 2. Normalized tearing eigenfunctions calculated for an ITER ohmically heated plasma interacting with an $m = 2/n = 1$ error-field. The vertical dotted line shows the location of the rational surface.

figure and can be seen to be strongly peaked. Of course, the strongly peaked current density profile is likely to be flattened in the plasma core by the sawtooth oscillation. We have neglected this effect in our calculation for the sake of simplicity. (The plasma core is of actually of little significance to error-field penetration studies because the relevant rational surfaces all lie in the outer regions of the plasma.) Finally, it is clear from the figure that the bootstrap current is negligible in both machines.

C. Example calculation

Consider the response of an ITER ohmically heated plasma to an $m = 2/n = 1$ tearing mode. The $2/1$ mode is such that $\hat{r}_s = 0.77$, $E_{ss} = -0.90$, and $E_{sb} = 2.2$ (see Sec. III). Note that the mode is tearing-stable (i.e., $E_{ss} < 0$). The normalized tearing eigenfunctions, $\hat{\psi}_s(\hat{r})$ and $\hat{\psi}_b(\hat{r})$, that characterize the plasma response to the error-field in the outer region are shown in Fig. 2 (see Sec. III C).

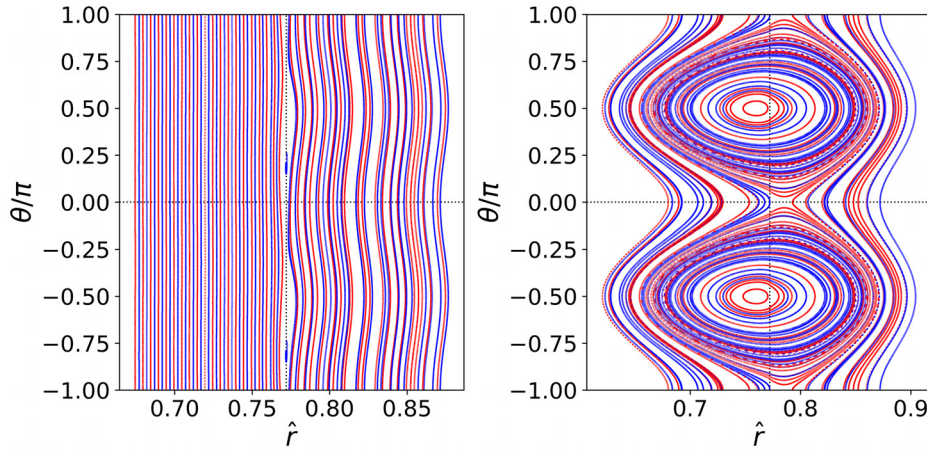


FIG. 3. Poincaré section of magnetic field-lines for an ITER ohmically heated plasma interacting with an $m = 2/n = 1$ error-field of normalized amplitude $\Psi_b = 1 \times 10^{-4}$ in the presence (left-hand panel) and in the absence (right-hand panel) of shielding. The vertical dotted lines show the location of the unperturbed rational surface.

Suppose, for the sake of example, that $l_E = +1$, which implies that the $\mathbf{E} \times \mathbf{B}$ frequency, ω_E , is equal to the electron diamagnetic frequency, ω_{*e} (This implies that the perpendicular ion fluid velocity is zero.) (see Sec. III L). The natural frequency, ω_0 , of the 2/1 tearing mode is defined as the frequency at which the mode would rotate, if it was tearing unstable.²¹ According to the well-established theory,^{23,24,57}

$$\omega_0 = \omega_E + \omega_{*e} = (1 + l_E)\omega_{*e}. \quad (183)$$

Incidentally, there is experimental evidence that, in ohmically heated tokamak plasmas, the natural frequency of tearing modes is in the electron diamagnetic direction, relative to the $\mathbf{E} \times \mathbf{B}$ frame, as predicted by the previous expression.⁵⁸

In our example calculation, we find that $\omega_0 = 1.3$ kHz. This frequency is well below the natural frequencies found in existing tokamaks, which are typically in excess of 10 kHz. The reason for the comparatively small natural frequency is the fact that ITER is significantly larger than existing tokamaks. (The natural frequency scales roughly as a^{-2} .) Given that the shielding of driven magnetic reconnection at the rational surface depends on the fact that the natural frequency is non-zero, we might suppose that this shielding is going to be comparatively weak in our example calculation. However, this is not the case because the estimated Lundquist number at the rational

surface is $S = 3.9 \times 10^8$. This value is much larger than that found in existing tokamaks. (Again, this is due to the fact that ITER is significantly larger than existing tokamaks.) It turns out that the factor that controls shielding at the rational surface is roughly proportional to $S^{1/3}\omega_0$ (see Sec. IV). Hence, the comparatively small natural frequency in our example calculation is offset by the comparatively large Lundquist number. Consequently, the shielding of driven magnetic reconnection is as large as if not larger than, that found in existing tokamaks. In fact, we estimate the shielding factor to be $\Sigma = 827$.

Suppose that the normalized amplitude of the 2/1 error-field is $\Psi_b = 1 \times 10^{-4}$ (see Sec. III F). This corresponds to an unshielded 2/1 radial magnetic field at the rational surface of $b_v/B_\phi = 2.0 \times 10^{-3}$. Figure 3 shows the Poincaré section of the magnetic field-lines in the vicinity of the 2/1 rational surface in the presence and in the absence of shielding. It can be seen that shielding profoundly modifies the response of the plasma to the error-field. In the absence of shielding, a comparatively wide magnetic island chain is driven at the rational surface. In the presence of shielding, this island chain is strongly suppressed.

Unfortunately, this is not the end of the story. The error-field exerts an electromagnetic torque at the rational surface that modifies the $\mathbf{E} \times \mathbf{B}$ frequency in such a manner that the natural frequency is reduced.^{21–24} Figure 4 shows the shielding factor and the natural

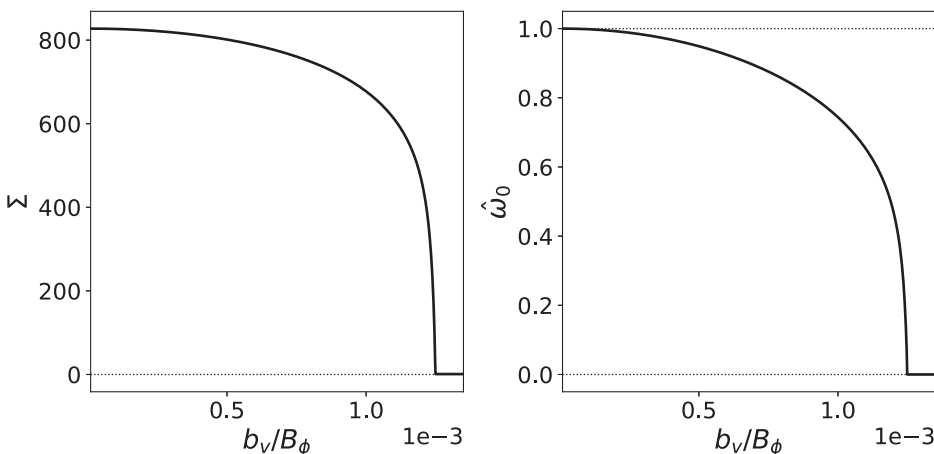


FIG. 4. The shielding factor, Σ , and the natural frequency divided by its value in the absence of an error-field, $\hat{\omega}_0$, calculated as functions of the error-field amplitude for an ITER ohmically heated plasma interacting with an $m = 2/n = 1$ error-field.

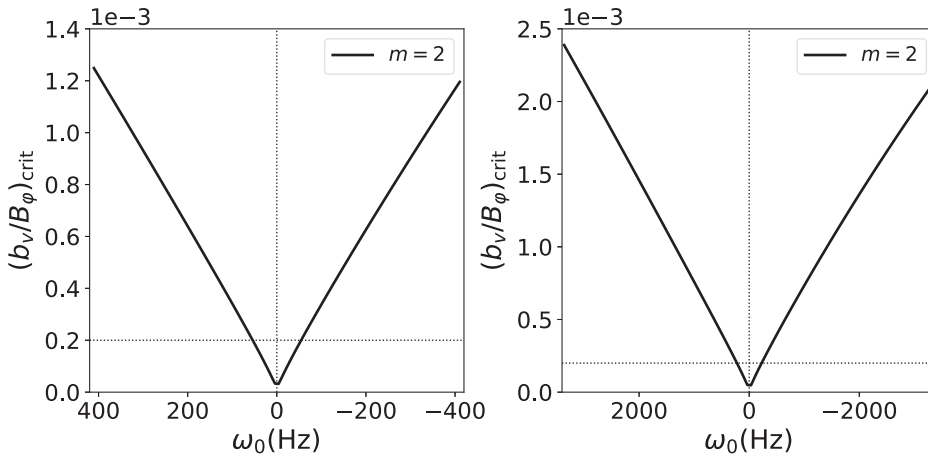


FIG. 5. The critical error-field amplitude for $n = 1$ error-field penetration as a function of the natural frequency. The left- and right-hand panels correspond to ITER and SPARC ohmically heated plasmas, respectively. The horizontal dotted lines show $(b_v/B_\phi)_{\text{crit}} = 2 \times 10^{-4}$.

frequency as functions of the error-field amplitude in our example calculation. It can be seen that as the error-field is (slowly) ramped up, the natural frequency is gradually reduced, but that, initially, this does not significantly modify the shielding factor. However, when the natural frequency has been reduced to about half of its original value, there is a sudden collapse in the natural frequency to a very small value, accompanied by a complete loss of shielding.^{21–24} It follows that the plasma response to the error-field suddenly transitions from that illustrated in the left-hand panel of Fig. 3 to that illustrated in the right-hand panel. As has already been mentioned, this phenomenon is known as error-field penetration and entails the sudden introduction of a comparatively wide locked magnetic island chain into the plasma at the rational surface. The critical unshielded 2/1 radial magnetic field at the rational surface needed to trigger penetration is $b_v/B_\phi = 1.2 \times 10^{-3}$.

D. Natural frequency scan

Figure 5 shows the critical $n = 1$ error-field amplitude needed to trigger error-field penetration (actually, it shows the critical error-field required to reduce the natural frequency to 1% of its original value), calculated as a function of the natural frequency, in ITER and SPARC

ohmically heated plasmas. Figure 6 shows the corresponding critical $n = 2$ error-field amplitudes. Finally, Fig. 7 shows the corresponding critical $n = 3$ error-field amplitudes. These calculations were performed by varying the parameter ι_E from +1 to -3, which implies a variation in the natural frequency from $+2 \omega_{*e}$ to $-2 \omega_{*e}$. This covers the likely range of natural frequencies in ITER and SPARC ohmically heated plasmas. A positive natural frequency corresponds to a tearing mode that would rotate in the electron diamagnetic direction, if it was naturally unstable. On the other hand, a negative natural frequency corresponds to a tearing mode that would rotate in the ion diamagnetic direction. Equivalently, a positive natural frequency corresponds to an electron fluid at the rational surface that rotates in the electron diamagnetic direction, whereas a negative natural frequency corresponds to an electron fluid that rotates in the ion diamagnetic direction.

Examining Figs. 5–7, it can be seen that the critical error-field amplitude needed to trigger error-field penetration attains a minimum value when the natural frequency, ω_0 , passes through zero. Note, however, that this minimum value is not zero. (The fact that the minimum value is not zero is an artifact of our definition of the critical error-field amplitude, namely, that it is the amplitude needed to require to reduce the natural frequency to 1% of its original value. In fact, the flat

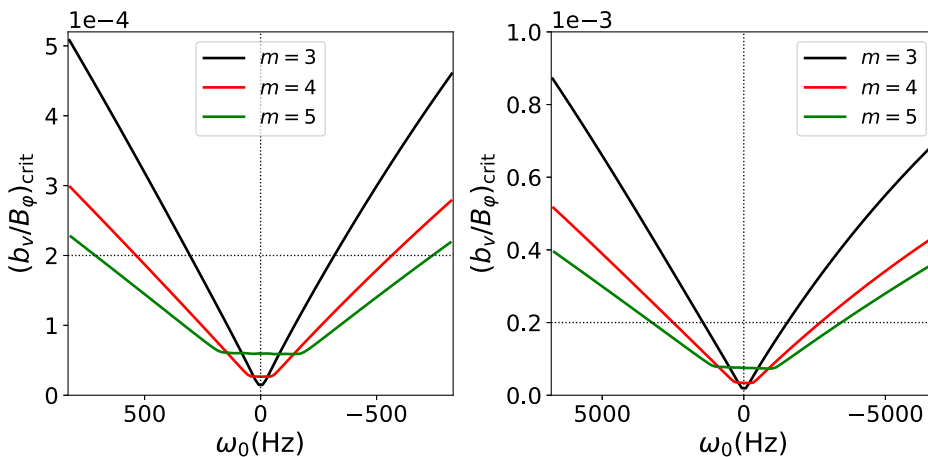


FIG. 6. The critical error-field amplitude for $n = 2$ error-field penetration as a function of the natural frequency calculated for various different poloidal mode numbers. The left- and right-hand panels correspond to ITER and SPARC ohmically heated plasmas, respectively. The horizontal dotted lines show $(b_v/B_\phi)_{\text{crit}} = 2 \times 10^{-4}$.

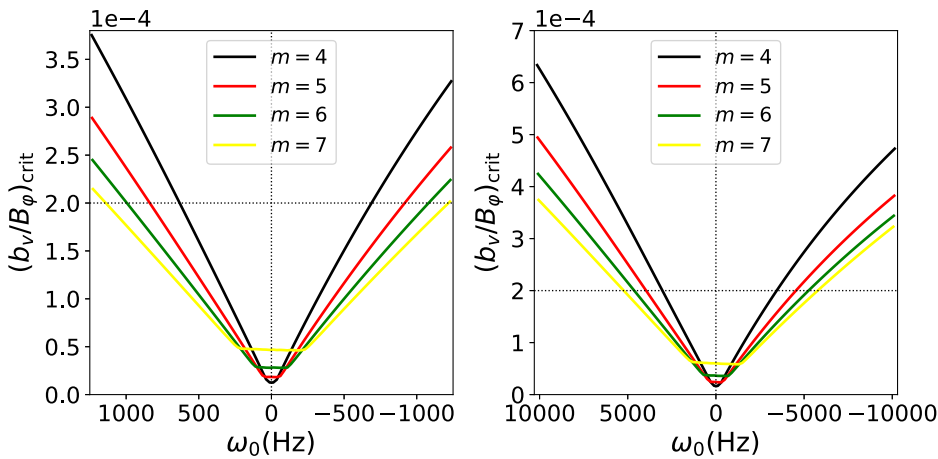


FIG. 7. The critical error-field amplitude for $n = 3$ error-field penetration as a function of the natural frequency calculated for various different poloidal mode numbers. The left- and right-hand panels correspond to ITER and SPARC ohmically heated plasmas, respectively. The horizontal dotted lines show $(b_v/B_\phi)_{crit} = 2 \times 10^{-4}$.

horizontal portions of the curves, where the natural frequency passes through zero, that can be seen in Figs. 5–7 correspond to the absence of effective shielding at the rational surface. It still takes a finite error-field amplitude to reduce the very small natural frequency to 1% of its original value, but the shielding has already disappeared.)

According to Figs. 6 and 7, the critical error-field amplitude needed to trigger error-field penetration decreases with increasing poloidal mode number. This is the case because rational surfaces with higher poloidal mode numbers are closer to the edge of the plasma, where the plasma is colder, and the Lundquist number is consequently smaller.

Figures 5–7 indicate a slight asymmetry between positive and negative natural frequencies for the case of an ITER and SPARC ohmically heated plasma. In other words, such plasmas are slightly more susceptible to error-field penetration when the electron fluid at the rational surface rotates in the ion diamagnetic direction, rather than in the electron diamagnetic direction.

On the basis of experience gained in past and existing tokamak experiments,^{1–5,8–10,12} the maximum likely value for an error-field in an ITER or a SPARC plasma is $b_v/B_\phi \simeq 2 \times 10^{-4}$. It is clear from Fig. 5 that, unless the natural frequency is very close to zero, the critical error-field amplitude needed to trigger $m = 2/n = 1$ error-field

penetration in an ITER or a SPARC ohmically heated plasma is significantly greater than this value. This suggests that diamagnetic levels of plasma rotation are sufficient to protect ITER and SPARC ohmically heated plasmas from $m = 2/n = 1$ error-field penetration.

Figures 6 and 7 show that the critical error-field amplitudes needed to trigger $n = 2$ or $n = 3$ error-field penetration in ITER and SPARC ohmically heated plasmas are not necessarily greater than $b_v/B_\phi \simeq 2 \times 10^{-4}$. This is especially the case for ITER. This suggests that ITER and SPARC ohmically heated plasmas may be vulnerable to $n > 1$ error-field penetration.

E. Electron number density scan

The calculations shown in Figs. 5–7 were all performed at the normal operating electron number densities for ITER and SPARC plasmas, namely, $n_e = 1 \times 10^{20} \text{ m}^{-3}$ for the case of ITER, and $n_e = 3 \times 10^{20} \text{ m}^{-3}$ for the case of SPARC. Let us examine what happens when the number density falls below the normal operating level, as might well be the case in the very early stages of an ohmically heated plasma. Figure 8 shows the critical error-field amplitude needed to trigger $m = 2/n = 1$ error-field penetration (again it, actually, shows the critical error-field required to reduce the natural frequency

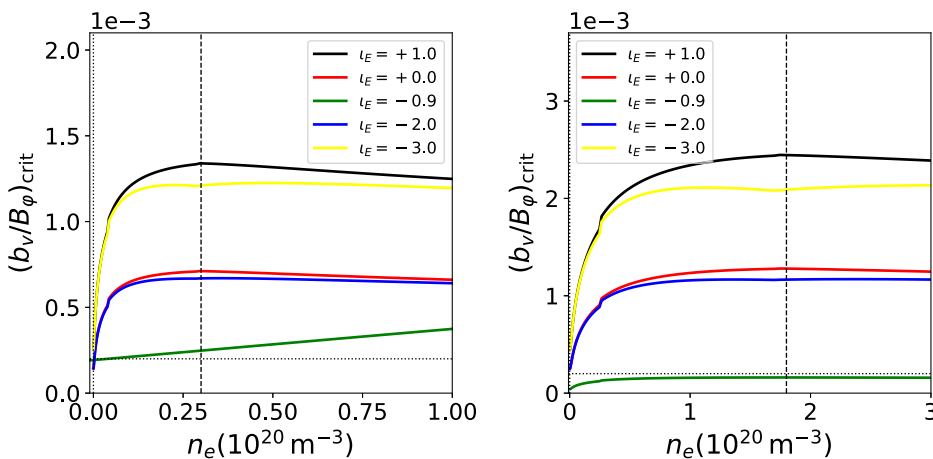


FIG. 8. The critical error-field amplitude for error-field penetration as a function of the electron number density calculated for various different values of t_E . The left- and right-hand panels correspond to ITER and SPARC ohmically heated plasmas, respectively. The dashed vertical lines indicate the critical electron number density above which the LOC confinement regime goes over to the SOC regime. The horizontal dotted lines show $(b_v/B_\phi)_{crit} = 2 \times 10^{-4}$.

to 1% of its original value), for various different values of t_E that span the likely range of variation of this parameter, calculated as a function of the electron number density, in ITER and SPARC ohmically heated plasmas.

According to Fig. 8, the critical error-field amplitude needed to trigger error-field penetration increases with increasing electron number density when the plasma lies in the low-density LOC regime. This increase has been observed in many tokamak experiments.^{1,3,4,6–11,13} (There is some debate in the literature as to whether the critical error-field amplitude scales as n_e^1 or as $n_e^{1/2}$. The results shown in Fig. 8 seem more consistent with an $n_e^{1/2}$ scaling.) On the other hand, as soon as the plasma enters the SOC regime, the increase in the critical error-field amplitude with increasing electron number density levels off. This roll-over has been observed in KSTAR plasmas.¹⁴ In our model, the increase in the critical error-field amplitude needed to trigger error-field penetration with increasing electron number density, at low electron number densities, is associated with the density dependence of the poloidal flow-damping rate. In other words, poloidal flow-damping becomes comparatively weak at low electron number densities (i.e., at high collisionality), which facilitates error-field penetration.

Figure 8 indicates that ITER and SPARC ohmically heated plasmas are only vulnerable to $m = 2/n = 1$ error-field penetration at electron number densities that are sufficiently low that the plasmas lie well inside the LOC regime.

VII. SUMMARY AND CONCLUSIONS

We have calculated the critical $n = 1$, $n = 2$, and $n = 3$ error-field amplitudes needed to trigger error-field penetration in ITER and SPARC, steady-state, ohmically heated plasmas. For the sake of simplicity, our model plasma equilibrium employs cylindrical geometry. However, we have endeavored to make the calculation of the Ohmic heating power as realistic as possible by taking into account plasma impurities, trapped particles, the bootstrap current, and the correction to the conventional cylindrical expression for the safety-factor due to toroidicity and plasma shaping. Our model energy confinement time is specified by the neo-Alcator scaling law in the low-density linear Ohmic confinement (LOC) regime and by the ITER-89P L-mode scaling law in the high-density saturated Ohmic confinement (SOC) regime. Our calculation employs a standard asymptotic matching approach. The response of the plasma in the outer region is calculated self-consistently from the cylindrical tearing mode equation. The response of the plasma in the inner region is calculated using a linearized version of the four-field model that incorporates $\mathbf{E} \times \mathbf{B}$ flows, electron and diamagnetic flows, the ion sound radius, and anomalous cross field energy and momentum diffusivity. Finally, the response of the plasma to the localized electromagnetic torque that develops in the inner region is calculated by solving the full plasma angular equations of motion, taking the neoclassical damping of poloidal rotation into account. The ultimate result is a torque balance equation that allows the local plasma flows, as well as the amount of reconnected magnetic flux driven at the rational surface, to be calculated as functions of the error-field amplitude.

We find that, at the normal operating electron number density, diamagnetic levels of rotation are sufficient to protect ITER and SPARC plasmas from $m = 2/n = 1$ error-field penetration. [This is essentially because the detrimental effect of comparatively low

(compared to existing tokamaks) rotation levels in such plasmas is offset by the beneficial effect of much larger Lundquist numbers.] On the other hand, SPARC, and especially ITER, ohmically heated plasmas may be vulnerable to $n > 1$ error-field penetration. ITER and SPARC ohmically heated plasmas are also found to be slightly more susceptible to error-field penetration when the electron fluid at the rational surface rotates in the ion diamagnetic direction, rather than the electron diamagnetic direction. Finally, at electron number densities that are sufficiently low that the plasma lies in the LOC confinement regime (such densities are well below the normal operating density), the error-field penetration threshold increases with increasing density. However, as soon as the electron number density becomes large enough that the plasma enters the SOC regime, the increase in the error-field penetration threshold with increasing density levels off.

ACKNOWLEDGMENTS

This research was directly funded by the U.S. Department of Energy, Office of Science, Office of Fusion Energy Sciences, under Contract No. DE-SC0021156.

AUTHOR DECLARATIONS

Conflict of Interest

The author has no conflicts to disclose.

Author Contributions

Richard Fitzpatrick: Conceptualization (lead); Formal analysis (lead); Funding acquisition (lead); Investigation (lead); Methodology (lead); Software (lead); Writing – original draft (lead); Writing – review & editing (lead).

DATA AVAILABILITY

The digital data used in the figures in this paper can be obtained from the corresponding author upon reasonable request.

REFERENCES

1. T. Scoville, R. J. LaHaye, A. G. Kellman, T. H. Osborne, R. D. Stambaugh, E. J. Strait, and T. S. Taylor, *Nucl. Fusion* **31**, 875 (1991).
2. R. J. LaHaye, R. Fitzpatrick, T. C. Hender, A. W. Morris, J. T. Scoville, and T. N. Todd, *Phys. Fluids B* **4**, 2098 (1992).
3. T. C. Hender, R. Fitzpatrick, A. W. Morris, P. G. Carolan, R. D. Durst, T. Edlington, J. Ferreira, S. J. Fielding, P. S. Haynes, J. Hugill *et al.*, *Nucl. Fusion* **32**, 2091 (1992).
4. G. M. Fishpool and P. S. Haynes, *Nucl. Fusion* **34**, 109 (1994).
5. R. J. Buttery, M. De' Benedetti, D. A. Gates, Y. Gribov, T. C. Hender, R. J. LaHaye, P. Leahy, J. A. Leuer, A. W. Morris, A. Santagiustina *et al.*, *Nucl. Fusion* **39**, 1827 (1999).
6. T. Scoville and R. J. La Haye, *Nucl. Fusion* **43**, 250 (2003).
7. R. C. Wolf, W. Biel, M. F. M. deBock, K. H. Finken, S. Günter, G. M. D. Hogeweijet, S. Jachmich, M. W. Jakubowski, R. J. E. Jaspers, A. Krämer-Flecken *et al.*, *Nucl. Fusion* **45**, 1700 (2005).
8. S. M. Wolfe, I. H. Hutchinson, R. S. Granetz, J. Rice, and A. Hubbard, *Phys. Plasmas* **12**, 056110 (2005).
9. D. F. Howell, T. C. Hender, and G. Cunningham, *Nucl. Fusion* **47**, 1336 (2007).
10. J. E. Menard, R. E. Bell, D. A. Gates, S. P. Gerhardt, J.-K. Park, S. A. Sabbagh, J. W. Berkery, A. Egan, J. Kallman, S. M. Kaye *et al.*, *Nucl. Fusion* **50**, 045008 (2010).

- ¹¹N. Wang, B. Rao, Q. Hu, Y. Ding, Z. Chen, L. Gao, W. Jin, B. Yi, W. Zeng, Q. Li *et al.*, *Nucl. Fusion* **54**, 064014 (2014).
- ¹²Y. In, J. K. Park, J. M. Jeon, J. Kim, and M. Okabayashi, *Nucl. Fusion* **55**, 043004 (2015).
- ¹³H.-H. Wang, Y.-W. Sun, T.-H. Shi, Q. Zang, Y.-Q. Liu, X. Yang, S. Gu, K.-Y. He, X. Gu, J.-P. Qian *et al.*, *Nucl. Fusion* **58**, 056024 (2018).
- ¹⁴S. M. Yang, J.-K. Park, Y. S. Na, Y. In, H. Hahn, J. W. Jeon, J. W. Yoo, W. H. Ko, K. D. Lee, J. H. Lee *et al.*, *Nucl. Fusion* **61**, 086009 (2021).
- ¹⁵P. C. de Vries, M. F. Johnson, B. Alper, P. Buratti, T. C. Hender, H. R. Koslowski, V. Riccardo, and JET-EFDA Contributors, *Nucl. Fusion* **51**, 053018 (2011).
- ¹⁶M. J. Lanctot, J.-K. Park, P. Piovesan, Y. Sun, R. J. Buttery, L. Frassinetti, B. A. Grierson, J. M. Hanson, S. R. Haskey, Y. In *et al.*, *Phys. Plasmas* **24**, 056117 (2017).
- ¹⁷T. E. Evans, R. A. Moyer, P. R. Thomas, J. G. Watkins, T. H. Osborne, J. A. Boedo, E. J. Doyle, M. E. Fenstermacher, K. H. Finken, R. J. Groebner *et al.*, *Phys. Rev. Lett.* **92**, 235003 (2004).
- ¹⁸Y. M. Jeon, J.-K. Park, S. W. Yoon, W. H. Ko, S. G. Lee, K. D. Lee, G. S. Yun, Y. U. Nam, W. C. Kim, J.-G. Kwak, K. S. Lee, H.-K. Kim, and H. L. Yang, *Phys. Rev. Lett.* **109**, 035004 (2012).
- ¹⁹W. Suttrop, T. Eich, J. C. Fuchs, S. Günter, A. Janzer, A. Herrmann, A. Kallenbach, P. T. Lang, T. Lunt, M. Maraschek, R. M. McDermott, A. Mlynek, T. Pütterich, M. Rott, T. Vierle, E. Wolftrum, Q. Yu, I. Zammuto, and H. Zohm, *Phys. Rev. Lett.* **106**, 225004 (2011).
- ²⁰A. Kirk, I. T. Chapman, Y. Liu, P. Cahyna, P. Denner, G. Fishpool, C. J. Ham, J. R. Harrison, Y. Liang, and E. Nardon, *Nucl. Fusion* **53**, 043007 (2013).
- ²¹R. Fitzpatrick, *Nucl. Fusion* **33**, 1049 (1993).
- ²²R. Fitzpatrick, *Phys. Plasmas* **5**, 3325 (1998).
- ²³A. Cole and R. Fitzpatrick, *Phys. Plasmas* **13**, 032503 (2006).
- ²⁴R. Fitzpatrick, *Phys. Plasmas* **29**, 032507 (2022).
- ²⁵R. Aymar, P. Barabaschi, and Y. Shimomura, *Plasma Phys. Controlled Fusion* **44**, 519 (2002).
- ²⁶A. J. Creely, M. J. Greenwald, S. B. Ballinger, D. Brunner, J. Canik, J. Doody, T. Fülöp, D. T. Garnier, R. Granetz, T. K. Gray *et al.*, *J. Plasma Phys.* **86**, 865860502 (2020).
- ²⁷N. C. Logan, J.-K. Park, Q. Hu, C. Paz-Solden, T. Markovic, H. Wang, Y. In, L. Piron, P. Piovesan, C. E. Mayers, M. Maraschek, S. M. Wolfe, E. J. Strait, and S. Munaretto, *Nucl. Fusion* **60**, 086010 (2020).
- ²⁸Q. Hu, N. C. Logan, J.-K. Park, C. Paz-Solden, R. Nazikian, and Q. Yu, *Nucl. Fusion* **60**, 076006 (2020).
- ²⁹P. N. Yushmanov, T. Takizuka, K. S. Riedel, O. J. W. F. Kardaun, J. G. Cordey, S. M. Kaye, and D. E. Post, *Nucl. Fusion* **30**, 1999 (1990).
- ³⁰J. E. Rice, N. M. Cao, T. Tala, C. Chrystal, M. J. Greenwald, J. W. Hughes, E. S. Marmor, M. L. Reinke, P. Rodriguez Fernandez, and A. Salmi, *Nucl. Fusion* **61**, 026013 (2021).
- ³¹S. P. Hirschman and D. J. Sigmar, *Nucl. Fusion* **21**, 1079 (1981).
- ³²Y. B. Kim, P. H. Diamond, and R. J. Groebner, *Phys. Fluids B* **3**, 2050 (1991).
- ³³ITER Physics Basis Editors *et al.*, *Nucl. Fusion* **39**, 2137 (1999).
- ³⁴S. Bingren, *Plasma Sci. Technol.* **5**, 1849 (2003).
- ³⁵R. J. Goldston, *Plasma Phys. Controlled Fusion* **26**, 87 (1984).
- ³⁶X. L. Zou, G. T. Hoang, L. Colas, L. Guizoui, and G. Bracco, in *Proceedings of 22nd EPS Conference on Controlled Fusion and Plasma Physics, Bournemouth, UK* (European Physical Society, 1995), p. 89.
- ³⁷J. E. Rice, J. Citrin, N. M. Cao, P. H. Diamond, M. Greenwald, and B. A. Grierson, *Nucl. Fusion* **60**, 105001 (2020).
- ³⁸R. D. Hazeltine, M. Kotschenreuther, and P. J. Morrison, *Phys. Fluids* **28**, 2466 (1985).
- ³⁹A. H. Glasser, J. M. Greene, and J. L. Johnson, *Phys. Fluids* **18**, 875 (1975).
- ⁴⁰A. H. Glasser, J. M. Greene, and J. L. Johnson, *Phys. Fluids* **19**, 567 (1976).
- ⁴¹H. Lütjens, J.-F. Luciani, and X. Garbet, *Phys. Plasmas* **8**, 4267 (2001).
- ⁴²X. Bai, Y. Liu, and Z. Gao, *Phys. Plasmas* **24**, 102505 (2017).
- ⁴³M. Kotschenreuther, R. D. Hazeltine, and P. J. Morrison, *Phys. Fluids* **28**, 294 (1985).
- ⁴⁴R. Fitzpatrick, *Phys. Fluids B* **1**, 2381 (1989).
- ⁴⁵R. Fitzpatrick, *Phys. Fluids B* **2**, 2636 (1990).
- ⁴⁶T. H. Stix, *Plasma Phys.* **14**, 367 (1972).
- ⁴⁷S. I. Braginskii, *Reviews of Plasma Physics* (Consultants Bureau, New York, 1965), Vol. I, p. 205.
- ⁴⁸R. Fitzpatrick, *Plasma Physics: An Introduction*, 2nd ed. (CRC Press, Boca Raton FL, 2022).
- ⁴⁹A. A. Galeev and R. Z. Sagdeev, *Sov. Phys. JETP* **23**, 233 (1968).
- ⁵⁰R. Fitzpatrick, *Phys. Plasmas* **30**, 042514 (2023).
- ⁵¹F. L. Hinton and C. Oberman, *Nucl. Fusion* **9**, 319 (1969).
- ⁵²J. Rice, "Intrinsic rotation and the residual stress Π_{res} ," in *Driven Rotation, Self-Generated Flow, and Momentum Transport in Tokamak Plasmas*, Springer Series on Atomic, Optical, and Plasma Physics, Vol. 119 (Springer, 2022).
- ⁵³M. F. F. Nave, E. Delabie, J. Ferreira, J. Garcia, D. King, M. Lennholm, B. Lomanowski, F. Parra, P. R. Fernandez *et al.*, *Nucl. Fusion* **63**, 044002 (2023).
- ⁵⁴H. P. Furth, J. Killeen, and M. N. Rosenbluth, *Phys. Fluids* **6**, 459 (1963).
- ⁵⁵D. P. Brennan, A. J. Cole, C. Akcay, and J. M. Finn, *Bul. Am. Phys. Soc.* **64**, 249 (2019).
- ⁵⁶J.-K. Park, *Phys. Plasmas* **29**, 072506 (2022).
- ⁵⁷G. Ara, B. Basu, B. Coppi, G. Laval, M. N. Rosenbluth, and B. V. Waddell, *Ann. Phys.* **112**, 443 (1978).
- ⁵⁸M. S. Chu, R. J. La Haye, M. E. Austin, L. L. Lao, E. Lazarus, A. Pletzer, C. Ren, E. J. Strait, T. S. Taylor, and F. L. Waelbroeck, *Phys. Plasmas* **9**, 4584 (2002).